Geophysical Research Letters

RESEARCH LETTER
10.1029/2026GL121893

Current and Future Changes in Earth's Outgoing Infrared Spectrum

J. K. Shaw[1,2], J. E. Kay[1,2], S. DeSouza-Machado[3], D. D. Turner[4], and L. L. Strow[3]

[1]Department of Atmospheric and Oceanic Sciences, University of Colorado Boulder, Boulder, CO, USA, [2]Cooperative Institute for Research in Environmental Science, University of Colorado Boulder, Boulder, CO, USA, [3]Joint Center for Earth Systems Technology/Physics Department, University of Maryland, Baltimore, MD, USA, [4]NOAA Global Systems Laboratory, Boulder, CO, USA

Key Points:

- Detectable trends in the current (2002–2024) AIRS spectral infrared record are dominated by CO_2 forcing and extratropical surface warming
- Observations from 2002 to 2042 will detect trends at some wavelengths where greenhouse gas forcing and temperature change currently compensate
- Detecting the breakdown of these compensations requires a multi-instrument, intercalibrated record with trend uncertainty below 0.02 K/yr

Supporting Information:

Supporting Information may be found in the online version of this article.

Correspondence to:

J. K. Shaw,
jonah.shaw@colorado.edu

Citation:

Shaw, J. K., Kay, J. E., DeSouza-Machado, S., Turner, D. D., & Strow, L. L. (2026). Current and future changes in Earth's outgoing infrared spectrum. *Geophysical Research Letters*, *53*, e2026GL121893. https://doi.org/10.1029/2026GL121893

Received 15 JAN 2026
Accepted 13 MAY 2026

Author Contributions:

Conceptualization: J. K. Shaw, J. E. Kay, D. D. Turner
Data curation: S. DeSouza-Machado, L. L. Strow
Formal analysis: J. K. Shaw
Funding acquisition: J. E. Kay
Investigation: J. K. Shaw
Methodology: J. K. Shaw
Resources: J. K. Shaw
Software: J. K. Shaw, S. DeSouza-Machado
Supervision: J. E. Kay
Validation: J. K. Shaw
Visualization: J. K. Shaw
Writing – original draft: J. K. Shaw

Abstract Hyperspectral infrared satellite observations provide an information-rich, global record of climate mean state and change without the structural uncertainties often present satellite retrievals and reanalyses. Current and planned hyperspectral satellite missions will continuously observe changes in Earth's outgoing infrared spectrum into the 2040s. Here, we study current and future changes in the infrared spectrum using 22 years of observations from the NASA AIRS instrument and 40 years of AIRS-like observations simulated in an Earth System Model. Currently detectable changes are dominated by CO_2 forcing and surface warming. Conversely, trends in spectral channels where CO_2 and water vapor forcing respectively oppose forced stratospheric and tropospheric temperature responses are indistinguishable from observed internal variability. By the early 2040s, however, mid-latitude stratospheric cooling and tropospheric warming outcompete greenhouse gas forcing to produce significant trends of opposing signs. Detecting these trends requires that the total uncertainty of a multi-instrument, intercalibrated record is below 0.02 K/yr.

Plain Language Summary Earth emits thermal infrared energy to space over a broad spectrum of wavelengths. Because greenhouse gases and temperature changes affect the amount of energy emitted at different wavelengths, monitoring changes in the infrared emission spectrum documents both the radiative forcings driving climate change as well as responding changes to the earth's atmosphere and surface. Examining 22 years of hyperspectral observations from the NASA AIRS instrument, we show that significant changes in the earth's emission spectrum are mostly due to just two factors: The radiative forcing of increasing carbon dioxide and surface temperature increases. By simulating future observations with a climate model, we show that additional radiative changes will become detectable during the next two decades. Specifically, cooling in the stratosphere will overcome CO_2 forcing, and warming in the troposphere will overcome decreasing emission due to increasing water vapor concentrations. Because future records will need to combine data from multiple satellites, however, detecting these trends in practice will require the precise intercalibration of multiple hyperspectral instruments.

1. Introduction

Anthropogenic climate change is the result of an imbalance between Earth's emission and absorption of radiative energy (Fourier, 1888). In the infrared spectrum where earth emits energy to space, the competing effects of radiative forcings and climate feedbacks give rise to a complex spectral and spatial signature of climate change and variability (e.g., Brindley & Bantges, 2016; Charlock, 1984; Goody et al., 1996). Space-based measurements of spectrally resolved infrared radiation observe how these processes evolve in time and contribute to the net radiative imbalance that drives climate change (e.g., Harries et al., 2001; Huang et al., 2022; Raghuraman et al., 2023). Assessing which changes current observations can and cannot detect, and estimating the benefits of future observations, is essential for both designing future observing systems and improving our understanding of climate processes.

Satellite-based spectral infrared observations offer unique advantages for climate-scale analysis, providing continuous, globe-spanning measurements of Earth's outgoing radiation. Since the first generation of weather satellites in the 1960s, infrared sounding capabilities have evolved dramatically in spectral resolution and accuracy. The launch of NASA's Atmospheric Infrared Sounder (AIRS) in 2002 marked a significant advancement, providing hyperspectral measurements across 2,378 infrared channels with unprecedented stability (Aumann et al., 2006; Chahine et al., 2006; Strow & DeSouza-Machado, 2020). AIRS observes across the 3.7–15.4 μm

Writing – review & editing: J. K. Shaw, J. E. Kay, S. DeSouza-Machado, D. D. Turner, L. L. Strow

(650–2,670 cm^{-1}) range, capturing information about temperature and humidity profiles as well as trace gas concentrations, aerosols, and clouds (Pagano et al., 2010). With AIRS now exceeding two decades of continuous operation, its spectral infrared record has matured into a valuable climate data record capable of detecting subtle changes in Earth's radiative forcing, atmospheric composition, and surface properties (e.g., Teixeira et al., 2024). Furthermore, the contribution of hyperspectral sounders to operational weather forecasting (e.g., Chahine et al., 2006) has motivated the launch of additional instruments (e.g., NASA's Cross-track Infrared Sounder (CrIS) and ESA's Infrared Atmospheric Sounding Interferometer (IASI)) that will create a continuous spectral infrared record of climate change and variability into the 2040s. While the primary purpose of these instruments is weather forecasting, inter-calibrated records joining multiple instruments such as the Climate Hyperspectral Infrared Radiance Product (CHIRP) will also provide valuable data for climate monitoring and trend detection (Strow et al., 2021).

Unlike traditional climate records that rely on derived geophysical variables, spectral radiances are direct observations of climate forcing and response. As a result, the uncertainty in long-term radiance trends can be directly tied to a satellite instrument's radiometric accuracy (Leroy et al., 2008; Wielicki et al., 2013). In the case of AIRS, Strow and DeSouza-Machado (2020) demonstrated that stable channels have trend uncertainties less than 0.002 Kyr^{-1}. This uncertainty is much smaller than expected trends from anthropogenic climate change, enabling the unambiguous detection of climate change signals. Satellite retrievals and atmospheric reanalyses, on the other hand, introduce additional sources of uncertainty from retrieval algorithms, forward model biases, and data assimilation methods. Reanalysis products in particular present challenges for climate analysis due to the changing observing systems they assimilate, which could introduce spurious trends and variability as satellite instruments enter and exit operations. Even climate data records derived from in situ observations can have large uncertainties that obscure and delay trend detection (e.g., Lenssen et al., 2024; J. Shaw & Lenssen, 2025; Sippel et al., 2024). Using radiance observations avoids these complications by leveraging the accuracy of direct spectral measurements.

Earth System Models (ESMs) coupled with satellite simulator tools can be used to simulate the observations of current and future satellite instruments (e.g., Bodas-Salcedo et al., 2011). At weather timescales, simulated radiances are often produced from operation weather models in Observing System Simulation Experiments (OSSEs) to assess the potential impact of new instruments on forecast skill (Hoffman & Atlas, 2016). At climate timescales, similar experiments can be used to assist the design of climate monitoring missions and provide strict tests of ESM performance (e.g., Feldman et al., 2011; Huang et al., 2007; Huang & Ramaswamy, 2009). Producing "satellite-like" radiation fields in ESMs requires additional radiative transfer calculations performed either in-line with model time steps or from saved model output (e.g., Raghuraman et al., 2023). While tools to support climate OSSEs are now available (e.g., Fera et al., 2023; J. K. Shaw et al., 2025), such experiments remain infrequent.

Previous studies have used the AIRS record both to document observed climate trends and to evaluate ESMs and reanalysis data products. Huang et al. (2007) and Huang and Ramaswamy (2009) respectively tested an ESM against AIRS observations and then predicted centennial-scale changes in the global-mean spectrum. Using globally averaged AIRS L1B radiances, Huang et al. (2022) found significant trends in channels sensitive to CO_2 and water vapor, with reanalysis disagreeing with observations in stratospheric and water vapor channels. Raghuraman et al. (2023) showed greenhouse gas (GHG) forcing, surface warming, stratospheric cooling using spectral outgoing longwave radiation (OLR) data from AIRS. Recently, DeSouza-Machado et al. (2025) infered geophysical trends directly from AIRS radiance trends and found the greatest disagreements relative to reanalyses and satellite retrievals in water vapor and polar stratospheric temperature trends. These studies demonstrate the value of spectral infrared observations for climate monitoring and model evaluation, especially for studying stratospheric temperature and water vapor changes where reanalyses, models, and satellite retrievals often disagree.

Here, we evaluate the current and future detectability of changes in Earth's infrared emission spectrum using 22 years of AIRS observations and simulated AIRS-like radiances extending into the mid-21st century. Previous work has focused on decomposing observed trends into various contributions (e.g., CO_2, temperature, humidity), largely at the global scale. In contrast, we examine spatial patterns of long-term trends and variability in the net signal that determines Earth's radiative imbalance. We use selected spectral channels that capture of the behavior of key parts of the infrared spectrum. We begin by examining how spatial patterns of variability and change

determine the detectability of climate change signals in different spectral regions. We then construct proxies of surface and atmospheric temperature trends from individual AIRS channels to understand current and future trends in regions where climate feedbacks and forcings have competing effects. Finally, we show the spectral and spatial regions where significant trends are expected to emerge over the next two decades and quantify the observational uncertainty threshold needed to detect these changes.

2. Methods

2.1. AIRS Observations

To leverage the AIRS record for climate change detection, we compute monthly mean radiances on a regular latitude-longitude grid from AIRS L1C orbit granules. The AIRS L1C spectral grid is drift-corrected and ideal for climate studies. Spatial grid spacing is 5° in longitude, with variable latitude spacing to give a roughly equal number of observations in each gridcell. We compute brightness temperatures from radiances to enable easier data interpretation and comparisons with temperature fields. Finally, we analyze observations for the 22-year period from September 2002 through August 2024. Monthly mean clear- and all-sky radiances separated by viewing geometry and orbit type for 470 AIRS L1C channels are publicly available as the Monthly AIRS Radiance (MAR) product, which this work also serves to document (J. Shaw et al., 2026).

We focus our analysis on clear-sky fields where spectral trends are readily interpreted (we reproduce figures with all-sky fields in the supplement). In the absence of a collocated cloud mask from another imager (e.g., MODIS), the choice of how to identify clear scenes is both non-trivial and ambiguous. We identify clear-sky observations following the methods of DeSouza-Machado et al. (2025). Namely, profiles with the greatest 10% of radiances in the 1,231 cm^{-1} window channel are labeled as clear-sky. This methodology has complete spatio-temporal coverage and uses direct observations rather than cloud-cleared radiances. However, caution is warranted in regions with frequent cloud cover and temperature inversions. Section S4 in Supporting Information S1 describes the extensive validation performed by DeSouza-Machado et al. (2025), and we refer readers to that work for full documentation.

Our analysis focuses on four spectral channels that capture the different patterns of trends and variability present in the AIRS record. These channels and their associated processes are: 659 cm^{-1} (CO_2 forcing and stratospheric temperature), 728 cm^{-1} (CO_2 forcing and tropospheric temperature), 1,231 cm^{-1} (surface temperature), and 1,596 cm^{-1} (water vapor and tropospheric temperature). Jacobians and weighting functions for each of these channels are shown in Figure S1 of Supporting Information S1. We limit our lat-lon analysis to these channels but note that the AIRS spectrum contains information on additional trace gases (e.g., CH_4, O_3).

2.2. CAM6 Experiment

We conduct a simulation with the Community Atmosphere Model version 6 (CAM6) to estimate internal climate variability and forced climate change in AIRS radiance fields over current and future observational periods. Specifically, we run CAM6 with CMIP6 forcings from the AMIP protocol from 2000 to 2014, and from the SSP5-8.5 scenario from 2015 onward (Eyring et al., 2016). We use sea surface temperature and sea ice boundary conditions from fully coupled Community Earth System Model version 2 (CESM2) (Danabasoglu et al., 2020) simulations with identical atmospheric forcings to drive atmosphere-only CAM6 experiments. We note that these boundary conditions diverge from observed fields in 2015 when the SSP5-8.5 scenario begins, and that our model simulation also has a different realization of atmospheric variability. Due to these differences and because both CAM6 and CESM2 have been extensively evaluated against both satellite observations and reanalysis (e.g., Medeiros et al., 2023; Simpson et al., 2020), our analysis focuses on trends and variability in the spectral radiation fields produced for this work.

We use the COSP-RTTOV satellite simulator tool (J. K. Shaw et al., 2025), which couples the COSPv2.0 satellite simulator package (Swales et al., 2018) with the RTTOV (Saunders et al., 2018) fast radiative transfer model and allows us to generate AIRS-like radiances from CAM6. COSP-RTTOV runs at each model timestep and uses the CAM6 model state to compute clear- and all-sky radiances consistent with AIRS L1C channel spectral response functions. We produce COSP-RTTOV output sampled at all timesteps, as well only 1:30p.m. and 1:30a.m. local times in order to study how the AIRS sun-synchronous sampling pattern influences our results. Specifically, we directly simulate 33 AIRS channels from 650 to 1,600 cm^{-1} (listed in Table S1 of Supporting Information S1).

For zonal-mean analysis, we use these directly simulated channels to reconstruct trends and variability across all L1C channels (Section S1, Figure S2 in Supporting Information S1). To compare with the AIRS observational period, we analyze CAM6 output from September 2002 through August 2024 (hereafter referred to as the current period). To study future trends, we extend the analysis period through August 2042 to examine 40-year trends that would be observed with seamless continuity of hyperspectral sounders (e.g., CrIS, IASI) (hereafter referred to as the future period). Finally, we interpolate model fields to the AIRS spatial grid to ensure fair comparison with observations.

2.3. Estimation of Trend Magnitude, Internal Climate Variability, and Trend Detection

We compute trends and variability analogously for AIRS observations and modeled fields to ensure fair comparison. We obtain linear trends by fitting monthly time series to the following model of a linear trend and seasonal cycle as in DeSouza-Machado et al. (2025):

$$\mathrm{BT}(t) = \mathrm{BT}_0 + m * t + \sum_{n=1}^{4} a_n \sin\left(2\pi t + \phi_n\right). \tag{1}$$

Here BT_0 is the climatological mean brightness temperature, m is the linear trend in K/yr, t is time in years since the middle of the record, and a_n and ϕ_n are the amplitude and phase of four sinusoids that fit the seasonal cycle, respectively. Fitting is performed using *scipy.optimize.curve_fit* (Virtanen et al., 2020).

While the linear trend m is obtained directly from the fit to Equation 1, we estimate trend variability (possible trends resulting from internal climate variability) from the residuals of the fit. Specifically, we assume that the residual variability behaves as a red-noise process with a stationary variance and autocorrelation structure. Following Weatherhead et al. (1998), trend standard error σ_m is computed as:

$$\sigma_m = \left[\frac{12}{T^3}\sigma_{\mathrm{var}}^2\,\tau_{\mathrm{var}}\right]^{1/2}, \tag{2}$$

where T is trend length, σ_{var} is the standard deviation of the residual variability, and τ_{var} is the correlation time of residual variability for time scales of 1 year and longer. We compute τ_{var} from the lag-1 autocorrelation ϕ of the residual variability following Weatherhead et al. (1998):

$$\tau_{\mathrm{var}} = \frac{1+\phi}{1-\phi}. \tag{3}$$

Trends are considered significant if the observed trend magnitude exceeds the quadrature sum of trend variability and instrument uncertainties. Following Strow and DeSouza-Machado (2020), we estimate the instrument trend uncertainty as 0.002 K/yr. Thus, trends are significant at 95% confidence if:

$$|m|^2 > (1.96\sigma_m)^2 + 0.002^2. \tag{4}$$

When considering future multi-instrument records for which intercalibration may increase observational uncertainty, we also compute a critical uncertainty threshold σ_{crit} at which observed trends lose significance:

$$\sigma_{\mathrm{crit}} = \left(|m|^2 - 1.96\sigma_m^2\right)^{1/2}. \tag{5}$$

2.4. Estimation of CO_2-Driven Trends

We wish to estimate and remove the contribution of increasing CO_2 concentrations to brightness temperature trends. Noting the logarithmic dependency of radiative forcing on gas concentration (Huang & Bani Shahabadi, 2014), we estimate the CO_2-driven brightness temperature trends by multiplying CO_2 trends with the sensitivity of brightness temperature to changes in CO_2 concentration (CO_2 Jacobians):

$$\frac{d\mathrm{BT}_{\mathrm{CO_2}}}{dt} = \frac{d\mathrm{BT}}{dln(\mathrm{CO_2})} \frac{dln(\mathrm{CO_2})}{dt}. \quad (6)$$

We account for state-dependency in Equation 6 by computing CO_2 Jacobians at each month and gridcell in our data using monthly mean atmospheric and surface fields (see Section S2 in Supporting Information S1). Figures S3 and S4 in Supporting Information S1 show that removing this CO_2 contribution from brightness temperature trends in CAM6 yields residual trends that agree well with the model's temperature fields, demonstrating that this approach allows us to isolate temperature-driven trends in channels where CO_2 forcing opposes the forced temperature response. Because these trends are assumed to be linear over the analysis periods, our estimates of internal variability and trend variability are unchanged.

Spatial and spectral variations in CO_2-driven trends (Figure S3 in Supporting Information S1) show how CO_2 forcing can be simply understood from the lapse rate at each wavelength's peak emission level. For example, positive CO_2-driven trends at 659 cm^{-1} decrease poleward as the stratospheric lapse rate weakens, while high-altitude regions have near-zero CO_2-driven trends at 728 cm^{-1} due to surface-dominated cooling in cold, dry atmospheres. These results confirm previous findings with simple models (e.g., Huang et al., 2016; Jeevanjee et al., 2021).

3. Results

We begin by evaluating zonal mean trends and variability in both observations and model data (Figure 1). Annotations to panels a and d label the spectral regions sensitive to changes in trace gases, atmospheric, and surface properties. AIRS observations (Figure 1a) show detectable trends (non-stippled regions) from CO_2 forcing (label 2), mid- and high-latitude surface warming (label 3), and CH_4 forcing (label 5). Conversely, changes in spectral regions where stratospheric temperatures trends oppose CO_2 forcing (label 1) and tropospheric temperatures trends oppose water vapor forcing (label 6) are largely insignificant over the 2002–2024 period. Modeled trends from CAM6 over the same period (Figure 1b) strongly resemble the observed fingerprint of spectral change. We note, however, that tropical surface temperature trends are larger and more significant in CAM6 than in AIRS. Future trends from CAM6 (Figure 1c) show little change in trend magnitude but greater trend significance: Surface warming is detected at all latitudes, while mid-latitude stratospheric and tropospheric temperature trends outcompete the respective radiative forcing of CO_2 and water vapor to emerge from internal variability.

The patterns of trend detectability in Figures 1a–1c are explained by additionally examining trend variability (Figures 1d–1f, Equation 2). Beginning with observations, variability derived from AIRS (Figure 1d) is greatest in spectral regions sensitive to stratospheric temperature, surface temperature at high latitudes, and water vapor in the tropics and extratropics. High variability in stratospheric channels (label 1) suppresses trend detectability, while low surface temperature variability in the southern hemisphere mid-latitudes allows for detectable trends despite more rapid warming in the northern hemisphere. As with trends, the CAM6 current period variability (Figure 1e) shows similar patterns to AIRS, though with some differences in magnitude. Lower surface temperature variability in CAM6 explains the greater detectability of tropical surface warming relative to AIRS. On the other hand, greater water vapor variability in CAM6 suppresses trend detectability. We note that differences in trends and variability arise from both model bias as well as internal climate variability. Finally, low variability in the CAM6 future period (Figure 1) shows that 20 years of additional observations dramatically reduce trend variability to enable more widespread trend detection in the extended AIRS record.

Further analysis of all-sky fields and temporal sampling patterns reinforces the results of Figure 1 while revealing additional features of the climate system. All-sky fields (Figure S5 in Supporting Information S1) shows largely similar results with greater variability in the tropics. Additionally, separating AIRS day- and nighttime orbits (Figures S11–S13 in Supporting Information S1) shows that nighttime observations detect additional surface warming trends due to larger trends and lower variability, with little change in other spectral regions. Additional results are discussed in Section S5 in Supporting Information S1.

We subsequently focus our analysis on four spectral channels representative of the key spectral regions identified in Figure 1. Global maps of observed trends and variability for these channels (Figure 2) show that regional trends are difficult to distinguish from internal variability over the observational period. Trends are mostly insignificant in channels sensitive to stratospheric temperatures, surface temperature, and water vapor (Figures 2a, 2b and 2d). Only the tropospheric temperature channel shows widespread negative and significant trends due to direct CO_2

10.1029/2026GL121893

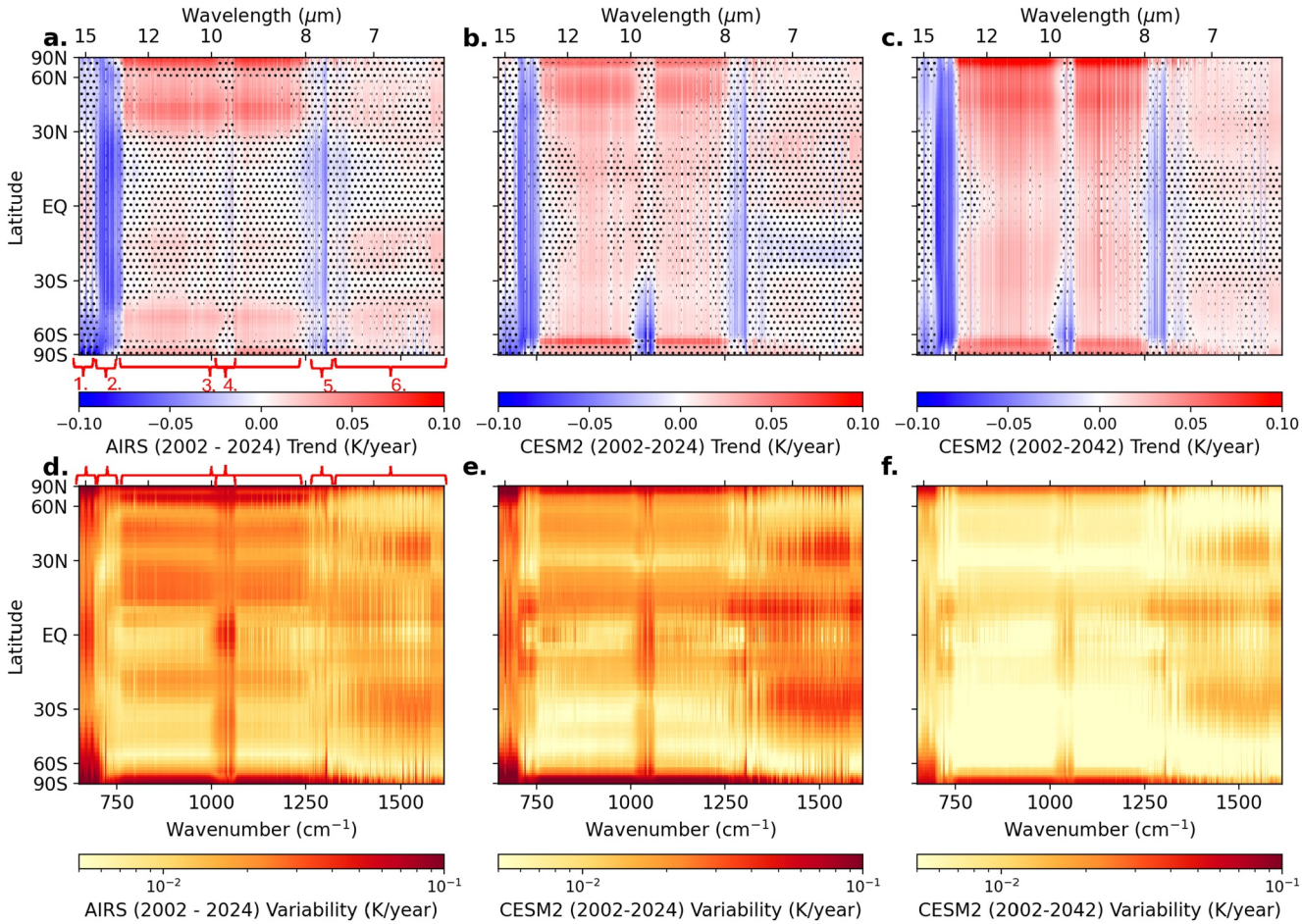

Figure 1. Zonal mean clear-sky brightness temperature trends (top row) and trend variability (bottom row) from the AIRS current observations (first column), CAM6 current simulation (second column), and CAM6 future simulation (third column). Trend variability is computed from detrended residuals as described in Section 2.3. Stippling in panels (a–c) indicates where trends do not exceed uncertainty calculated with Equation 4. Annotations to panels a and d label the spectral regions sensitive to changes in 1. Stratospheric temperature and CO_2 (650–700 cm^{-1}), 2. Tropospheric temperature and CO_2 (700–750 cm^{-1}), 3. Surface temperature (750–1,000, 1,050–1,250 cm^{-1}), 4. Ozone (1,000–1,050 cm^{-1}), 5. CH_4 (1,250–1,400 cm^{-1}), and 6. Water vapor and Tropospheric temperature (1,400–1,600 cm^{-1}).

forcing (Figure 2c). When the inferred CO_2 contributions are removed from CO_2-sensitive channels, however, the sign of the residual trend (now due only to the temperature response) is reversed. Stratospheric cooling in the tropics drives a negative trend at 659 cm^{-1} (Figure 2e) while tropospheric warming drives a significant positive trend at 728 cm^{-1} (Figure 2f). The patterns of trend detection (Figure 2, non-stippled regions) are largely controlled by spatial patterns of variability. Temperature variability in surface-, troposphere-, and stratosphere-sensitive channels increases from the equator to the poles, causing most significant trends to occur in the tropics and mid-latitudes (Figures 2g–2i). In contrast with temperature, variability in the water vapor channel (Figure 2j) is greatest in the tropics due to the Clausius-Clapeyron relationship. Overall, Figure 2 shows that detectable trends in individual gridcells result from CO_2 radiative forcing and high-latitude surface warming. Trends in other spectral and spatial regions are largely indistinguishable from internal variability. Figure S6 in Supporting Information S1 shows model behavior over the same period.

Extending the AIRS record to 40 years with CAM6 shows that regionally detectable spectral trends become common and spatially widespread (Figure 3). In this extended record, CO_2 forcing and surface warming remain the dominant, robust signals (Figures 3a and 3c), while mid-latitude stratospheric cooling and tropospheric warming emerge more broadly as detectable trends (Figures 3b and 3d). In the tropics, however, trends in stratospheric and water vapor channels remain largely insignificant: in the stratospheric band CO_2 forcing and the cooling response approximately cancel, and in the water vapor band opposing temperature and humidity effects combined with large trend variability suppress detectability. Because 40-year trend variability is reduced relative

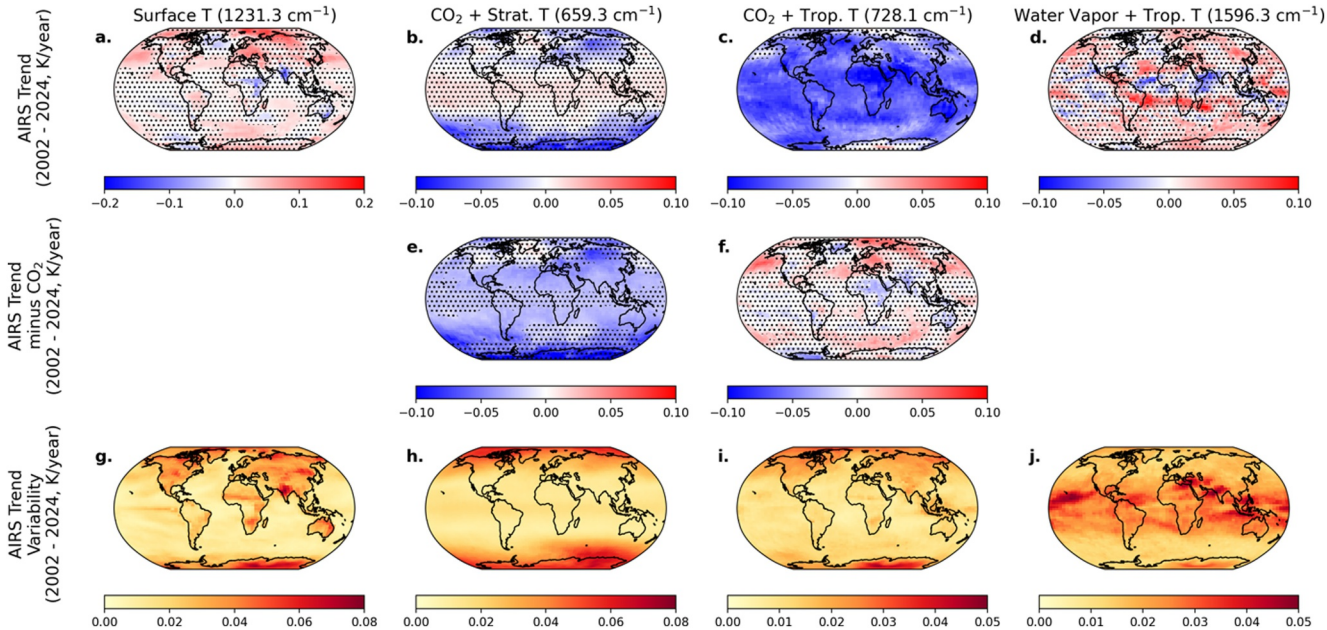

Figure 2. Clear-sky brightness temperature trends (top row), trends with inferred CO_2 contributions removed (middle row), and trend variability (bottom row) from AIRS current observations (2002–2024) for four representative spectral channels. Stippling in panels (a–f) indicates where trends do not exceed uncertainty calculated with Equation 4.

to the shorter observational period (Figures 3g–3j), smaller forced signals cross the detection threshold. Comparing Figures 2 and 3 shows that a continuous hyperspectral record from 2002 to 2042 would reveal additional changes in Earth's infrared spectrum.

Our assumption that the AIRS radiometric stability will be seamlessly transferred to a multi-instrument record may be optimistic. To understand the long-term uncertainty needed to maintain the trend detection shown in

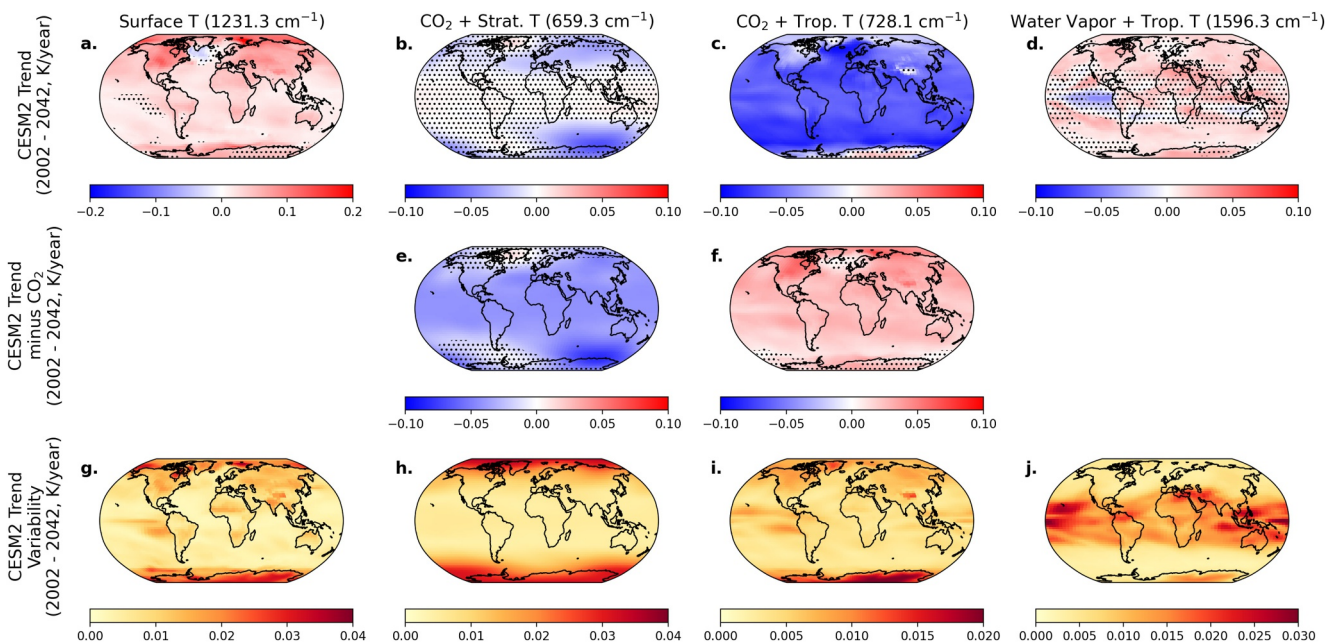

Figure 3. Clear-sky brightness temperature trends (top row), trends with inferred CO_2 contributions removed (middle row), and trend variability (bottom row) from CAM future simulation (2002–2042) for four representative spectral channels. Stippling in panels (a–f) indicates where trends do not exceed uncertainty calculated with Equation 4.

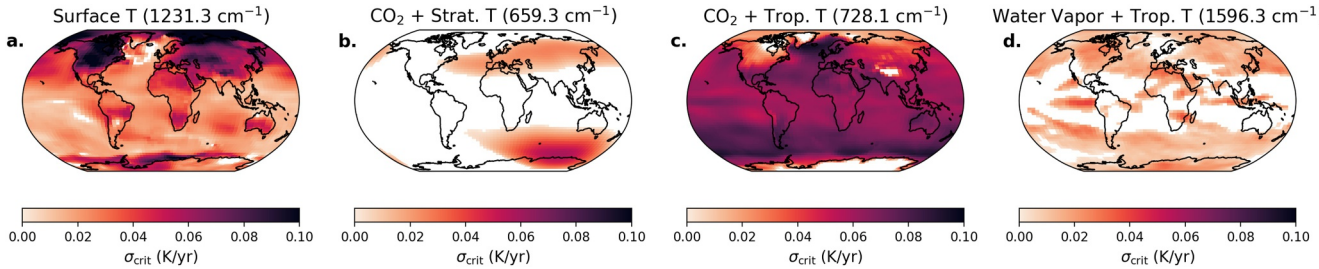

Figure 4. Critical uncertainty σ_{crit} calculated following Equation 5 using CAM future simulation (2002–2042) for four representative AIRS spectral channels. Higher values of σ_{crit} indicate that trends remain significant even with larger observational uncertainties. Missing values in white indicate regions where trends are not significant even with zero observational uncertainty.

Figure 3, we compute the critical uncertainty σ_{crit} (Equation 5) of trend detection for the CAM6 future simulation (Figure 4). Higher values of σ_{crit} indicate that trends remain significant even with larger observational uncertainties. As expected, the CO_2 forcing and surface temperature dominated trends are robust to observational uncertainty and have the highest σ_{crit} values (Figures 4a and 4c). The detection of trends in the stratospheric temperature and water vapor channels, however, is more sensitive to observational uncertainty (Figures 4b and 4d). In particular, detection of trends in the water vapor channel requires observational uncertainties to remain below 0.02 K/year in most regions. Detection before 2042 would require smaller uncertainties.

4. Discussion and Conclusion

In this study, we examined current and future trends in spectral infrared radiation using satellite observations and climate model simulations. We showed that current (2002–2024) observations from the NASA AIRS instrument detect trends due to CO_2 forcing and extra-tropical surface warming, but that trends in other spectral and spatial regions are largely indistinguishable from internal climate variability (Figures 1a and 2). In contrast, future (2002–2042) trends simulated by CAM6 are detected in additional spectral regions where temperature and greenhouse gas-driven changes oppose each other (Figure 1c). These "to-be-detected" trends break the approximate compensation between CO_2 forcing and stratospheric cooling (659 cm^{-1} channel) as well as water vapor forcing and tropospheric warming (1,596 cm^{-1} channel) that have been recently observed (e.g., Raghuraman et al., 2023).

Decomposing observed trends into contributions from CO_2 forcing and temperature response reveals that trends from tropospheric and stratospheric temperature changes alone often exceed internal variability but the observed signal is masked by greenhouse gas forcing (Figure 2). These results are consistent with previous studies that have decomposed spectral radiation trends (Huang et al., 2022; Raghuraman et al., 2023). We show that future observations, however, are able to detect imbalances in these spectral compensations as temperature-driven trends outcompete greenhouse gas forcing in the mid-latitudes (Figures 1 and 3). This feature, first suggested by the 100-year changes simulated by Y. Huang and Ramaswamy (2009), is now visible in the zonal average for water vapor channels but not stratospheric CO_2 channels (Figure 1a).

Three of the four spectral channels studied here have earliest trend detection in the mid-latitudes. Not only are surface warming trends most significant in the mid-latitudes (Figure 1), but future trends in the CO_2 and stratospheric temperature (659 cm^{-1}) and water vapor and tropospheric temperature (1,596 cm^{-1}) channels are also expected to emerge in the mid-latitudes (Figure 3). This early detection occurs in the mid-latitudes due to a combination of low variability and moderate trends, similar to the fall season detection of broadband OLR changes in the Arctic (J. K. Shaw & Kay, 2023). Furthermore, the 659 and 1,596 cm^{-1} channels have trends of opposite sign, implying that the breakdown of the temperature versus forcing balance in these spectral regions may itself be compensated for when integrating across the infrared spectrum. Indeed, two recent studies show that the broadband longwave trends are determined by water vapor absorption. Huang and Huang (2024) show that low compensation from water vapor allows strong radiative cooling from the Arctic while Hirose et al. (2025) show that a transition from negative to positive OLR trends near 30°N is controlled by competing water vapor and tropospheric temperature changes. Additional compensation from the 659 cm^{-1} region is unstudied, and observed trends are undetected.

Fair comparisons of clear-sky scenes remain a challenge. First, COSP-RTTOV produces clear-sky radiation fields by removing all cloud condensate from radiative transfer calculations. This common modeling approach does not modify variables that covary with cloud amount, introducing a definitional difference with clear-sky satellite observations. This likely causes an overestimation of variability in the water vapor sensing region in CAM6 (Figure 2 and Figure S6 in Supporting Information S1) and delays trend detection. Multiple clear-sky radiation fields from the NASA Clouds and the Earth's Radiant Energy System (CERES) record (Kato et al., 2025; Team, 2023) quantify the impact of this difference in the broadband, and work is ongoing to add similar functionality to COSP-RTTOV. Additionally, our simple cloud-clearing methodology is susceptible to contamination and would be improved by a MODIS cloud mask colocated to AIRS footprints. Reproducing all figures using all-sky fields (Figures S5, S8–S10 in Supporting Information S1), however, shows that increased variability from clouds delays some trend detection and lowers critical uncertainty values, but our main results are unchanged.

Two additional decades of observations aid detection by reducing trend variability; changes in the magnitude and pattern of trends are less important. Recognizing the importance of trend uncertainty, we determine the critical observational uncertainty required for future multi-instrument records to maintain trend detectability (Figure 4). While trends in surface and tropospheric temperature channels are robust to potential increases in observational uncertainty from intercalibration, detecting trends in water vapor channels requires observational uncertainties to remain below at least 0.02 K/year in most regions. Because expected intercalibration uncertainty is below this threshold, changes will likely detectable earlier. The use of hyperspectral records for long-term climate monitoring and analysis is especially important given the potential loss of continuity in the broadband radiation record (Loeb et al., 2024).

Overall, our results show that changes in Earth's surface and atmosphere are causing detectable changes across the infrared spectrum. As the satellite record extends into the mid-21st century, spectral regions currently offset by greenhouse gas forcing and masked by internal variability will reveal unmistakable signs of climate change. Specifically, stratospheric cooling and tropospheric warming will modify the current pattern of spectral change that is dominated by direct CO_2 forcing and the surface temperature response. Maintaining high-precision intercalibration between successive hyperspectral instruments is needed to confirm these model predictions and interrogate the underlying physics of the climate system.

Acknowledgments
The authors thank two anonymous reviewers for thoughtful, constructive feedback during the review process. JKS and JEK were supported by NASA PREFIRE mission award no. 849K995. JKS was additionally supported by NASA FINESST Grant 80NSSC22K1. This publication is funded in part by the Gordon and Betty Moore Foundation through Grant GBMF13925 to JEK to support the work of JKS. Computing and data storage resources, including the Derecho (https://doi.org/10.5065/qx9a-pg09; Computational and Information Systems Laboratory, 2023) supercomputer, were provided by the Computational and Information Systems Laboratory of the National Science Foundation's National Center for Atmospheric Research (NSF NCAR). JKS thanks the Polar Climate Working Group of the Community Earth System Model for computing resources. JKS additionally thanks James Hocking and the RTTOV development team for producing RTTOV coefficients for the AIRS L1C spectral grid. The scientific results and conclusions, as well as any views or opinions expressed herein, are those of the author(s) and do not necessarily reflect those of NASA, NSF, NOAA, or the Department of Commerce. Large Language Model tools (Github Copilot) were used in figure creation and manuscript editing.

Conflict of Interest

The authors declare no conflicts of interest relevant to this study.

Availability Statement

Data and code to reproduce figures can be found at: (J. Shaw, 2026). COSP-RTTOV source code can be found at (J. Shaw, 2025). The Monthly AIRS Radiance (MAR) data set can be found at (J. Shaw et al., 2026). CAM6 source code with RTTOV integration can be found at: (J. Shaw et al., 2026).

References

Aumann, H., Broberg, S., Elliott, D., Gaiser, S., & Gregorich, D. (2006). Three years of atmospheric infrared sounder radiometric calibration validation using sea surface temperatures. *Journal of Geophysical Research*, *111*(D16). https://doi.org/10.1029/2005jd006822

Bodas-Salcedo, A., Webb, M. J., Bony, S., Chepfer, H., Dufresne, J. L., Klein, S. A., et al. (2011). COSP: Satellite simulation software for model assessment. *Bulletin of the American Meteorological Society*, *92*(8), 1023–1043. https://doi.org/10.1175/2011BAMS2856.1

Brindley, H., & Bantges, R. (2016). The spectral signature of recent climate change. *Current Climate Change Reports*, *2*(3), 112–126. https://doi.org/10.1007/s40641-016-0039-5

Chahine, M. T., Pagano, T. S., Aumann, H. H., Atlas, R., Barnet, C., Blaisdell, J., et al. (2006). AIRS: Improving weather forecasting and providing new data on greenhouse gases. *Bulletin of the American Meteorological Society*, *87*(7), 911–926. https://doi.org/10.1175/BAMS-87-7-911

Charlock, T. P. (1984). CO_2 induced climatic change and spectral variations in the outgoing terrestrial infrared radiation. *Tellus B: Chemical and Physical Meteorology*, *36*(3), 139–148. https://doi.org/10.1111/j.1600-0889.1984.tb00236.x

Danabasoglu, G., Lamarque, J. F., Bacmeister, J., Bailey, D. A., DuVivier, A. K., Edwards, J., et al. (2020). The community earth system model version 2 (CESM2). *Journal of Advances in Modeling Earth Systems*, *12*(2), e2019MS001916. https://doi.org/10.1029/2019MS001916

DeSouza-Machado, S., Strow, L. L., & Kramer, R. J. (2025). Geophysical trends inferred from 20 years of airs infrared global observations. *Journal of Geophysical Research: Atmospheres*, *130*(15), e2025JD043501. https://doi.org/10.1029/2025JD043501

Eyring, V., Bony, S., Meehl, G. A., Senior, C. A., Stevens, B., Stouffer, R. J., & Taylor, K. E. (2016). Overview of the coupled model intercomparison project phase 6 (CMIP6) experimental design and organization. *Geoscientific Model Development*, *9*(5), 1937–1958. https://doi.org/10.5194/GMD-9-1937-2016

Feldman, D. R., Algieri, C. A., Collins, W. D., Roberts, Y. L., & Pilewskie, P. A. (2011). Simulation studies for the detection of changes in broadband albedo and shortwave nadir reflectance spectra under a climate change scenario. *Journal of Geophysical Research*, *116*(D24), 24103. https://doi.org/10.1029/2011JD016407

Fera, S. D., Fabiano, F., Raspollini, P., Ridolfi, M., Cortesi, U., Barbara, F., & Hardenberg, J. V. (2023). On the use of infrared atmospheric sounding interferometer (IASI) spectrally resolved radiances to test the Ec-earth climate model (v3.3.3) in clear-sky conditions. *Geoscientific Model Development*, *16*(4), 1379–1394. https://doi.org/10.5194/GMD-16-1379-2023

Fourier, J. B. J. (1888). *Théorie analytique de la chaleur*. Gauthier-Villars et fils.

Goody, R., Haskins, R., Abdou, W., & Chen, L. (1996). Detection of climate forcing using emission spectra. *Earth Observation and Remote Sensing*, *13*(5), 713–727.

Harries, J. E., Brindley, H. E., Sagoo, P. J., & Bantges, R. J. (2001). Increases in greenhouse forcing inferred from the outgoing longwave radiation spectra of the Earth in 1970 and 1997. *Nature*, *410*(6826), 355–357. https://doi.org/10.1038/35066553

Hirose, L. A., Paynter, D., Menzel, R., & Ramaswamy, V. (2025). Latitudinal differences of changes in northern hemisphere clear-sky outgoing longwave radiation over the past 4 decades (1979–2021). *Environmental Research Letters*, *20*(10), 104053. https://doi.org/10.1088/1748-9326/ae0500

Hoffman, R. N., & Atlas, R. (2016). Future observing system simulation experiments. *Bulletin of the American Meteorological Society*, *97*(9), 1601–1616. https://doi.org/10.1175/BAMS-D-15-00200.1

Huang, H., & Huang, Y. (2024). Arctic as the "radiator fins" of Earth in a warming climate. *Environmental Research Letters*, *19*(5), 054032. https://doi.org/10.1088/1748-9326/ad3e17

Huang, X., Chen, X., Fan, C., Kato, S., Loeb, N., Bosilovich, M., et al. (2022). A synopsis of AIRS global-mean clear-sky radiance trends from 2003 to 2020. *Journal of Geophysical Research: Atmospheres*, *127*(24), e2022JD037598. https://doi.org/10.1029/2022JD037598

Huang, Y., & Bani Shahabadi, M. (2014). Why logarithmic? A note on the dependence of radiative forcing on gas concentration. *Journal of Geophysical Research: Atmospheres*, *119*(24), 13683–13689. https://doi.org/10.1002/2014JD022466

Huang, Y., & Ramaswamy, V. (2009). Evolution and trend of the outgoing longwave radiation spectrum. *Journal of Climate*, *22*(17), 4637–4651. https://doi.org/10.1175/2009JCLI2874.1

Huang, Y., Ramaswamy, V., Huang, X., Fu, Q., & Bardeen, C. (2007). A strict test in climate modeling with spectrally resolved radiances: GCM simulation versus AIRS observations. *Geophysical Research Letters*, *34*(24). https://doi.org/10.1029/2007GL031409

Huang, Y., Tan, X., & Xia, Y. (2016). Inhomogeneous radiative forcing of homogeneous greenhouse gases. *Journal of Geophysical Research: Atmospheres*, *121*(6), 2780–2789. https://doi.org/10.1002/2015JD024569

Jeevanjee, N., Seeley, J. T., Paynter, D., & Fueglistaler, S. (2021). An analytical model for spatially varying clear-sky CO_2 forcing. *Journal of Climate*, *34*(23), 9463–9480. https://doi.org/10.1175/JCLI-D-19-0756.1

Kato, S., Loeb, N. G., Rose, F. G., Ham, S. H., Thorsen, T. J., Rutan, D. A., et al. (2025). Seamless continuity in Ceres energy balanced and filled (EBAF) surface radiation budget across multiple satellites. *Journal of Climate*, *38*(11), 2461–2478. https://doi.org/10.1175/JCLI-D-23-0568.1

Lenssen, N., Schmidt, G. A., Hendrickson, M., Jacobs, P., Menne, M. J., & Ruedy, R. (2024). A NASA GISTEMPv4 observational uncertainty ensemble. *Journal of Geophysical Research: Atmospheres*, *129*(17), e2023JD040179. https://doi.org/10.1029/2023JD040179

Leroy, S. S., Anderson, J. G., & Ohring, G. (2008). Climate signal detection times and constraints on climate benchmark accuracy requirements. *Journal of Climate*, *21*(4), 841–846. https://doi.org/10.1175/2007JCLI1946.1

Loeb, N. G., Doelling, D. R., Kato, S., Su, W., Mlynczak, P. E., & Wilkins, J. C. (2024). Continuity in top-of-atmosphere Earth radiation budget observations. *Journal of Climate*, *37*(23), 6093–6108. https://doi.org/10.1175/jcli-d-24-0180.1

Medeiros, B., Shaw, J., Kay, J. E., & Davis, I. (2023). Assessing clouds using satellite observations through three generations of global atmosphere models. *Earth and Space Science*, *10*(7), e2023EA002918. https://doi.org/10.1029/2023EA002918

Pagano, T. S., Chahine, M. T., & Fetzer, E. J. (2010). The atmospheric infrared sounder (airs) on the NASA aqua spacecraft: A general remote sensing tool for understanding atmospheric structure, dynamics, and composition. *Remote sensing of clouds and the atmosphere xv*, *7827*, 162–169.

Raghuraman, S. P., Paynter, D., Ramaswamy, V., Menzel, R., & Huang, X. (2023). Greenhouse gas forcing and climate feedback signatures identified in hyperspectral infrared satellite observations. *Geophysical Research Letters*, *50*(24), e2023GL103947. https://doi.org/10.1029/2023GL103947

Saunders, R., Hocking, J., Turner, E., Rayer, P., Rundle, D., Brunel, P., et al. (2018). An update on the RTTOV fast radiative transfer model (currently at version 12). *Geoscientific Model Development*, *11*(7), 2717–2737. https://doi.org/10.5194/GMD-11-2717-2018

Shaw, J. (2025). *jshaw35/COSPv2.0: COSP-RTTOV-1.0*. Dataset on Zenodo. https://doi.org/10.5281/ZENODO.14750169

Shaw, J. (2026). Data and code for "Current and Future Changes in Earth's Outgoing Infrared Spectrum". *Zenodo*. https://doi.org/10.5281/zenodo.18167283

Shaw, J., & Lenssen, N. (2025). Early and widespread emergence of regional warming is robust to observational and model uncertainty. *Environmental Research Letters*, *20*(7), 074066. https://doi.org/10.1088/1748-9326/ADE458

Shaw, J., Peverley, C., cacraigucar, Nusbaumer, J., & goldy (2026). Jshaw35/CAM: COSP-RTTOV for CESM2.1.5. *Zenodo*. https://doi.org/10.5281/zenodo.19462673

Shaw, J., Strow, L., & DeSouza-Machado, S. (2026). MAR: Monthly Airs Radiances (2002-09 through 2024-08). *Zenodo*. https://doi.org/10.5281/zenodo.18110441

Shaw, J. K., & Kay, J. E. (2023). Processes controlling the seasonally varying emergence of forced arctic longwave radiation changes. *Journal of Climate*, *36*(20), 7337–7354. https://doi.org/10.1175/JCLI-D-23-0020.1

Shaw, J. K., Swales, D. J., DeSouza-Machado, S., Turner, D. D., Kay, J. E., & Schneider, D. P. (2025). Cosp-Rttov-1.0: Flexible radiation diagnostics to enable new science applications in model evaluation, climate change detection, and satellite mission design. *Geoscientific Model Development*, *18*(15), 4935–4950. https://doi.org/10.5194/gmd-18-4935-2025

Simpson, I. R., Bacmeister, J., Neale, R. B., Hannay, C., Gettelman, A., Garcia, R. R., et al. (2020). An evaluation of the large-scale atmospheric circulation and its variability in CESM2 and other CMIP models. *Journal of Geophysical Research: Atmospheres*, *125*(13), e2020JD032835. https://doi.org/10.1029/2020JD032835

Sippel, S., Kent, E. C., Meinshausen, N., Chan, D., Kadow, C., Neukom, R., et al. (2024). Early-twentieth-century cold bias in ocean surface temperature observations. *Nature 2024*, *635*(8039), 618–624. https://doi.org/10.1038/s41586-024-08230-1

Strow, L. L., & DeSouza-Machado, S. (2020). Establishment of AIRS climate-level radiometric stability using radiance anomaly retrievals of minor gases and sea surface temperature. *Atmospheric Measurement Techniques*, *13*(9), 4619–4644. https://doi.org/10.5194/AMT-13-4619-2020

Strow, L. L., Hepplewhite, C., Motteler, H., Buczkowski, S., & Desouza-Machado, S. (2021). A climate hyperspectral infrared radiance product (CHIRP) combining the AIRS and CrIS satellite sounding record. *Remote Sensing 2021*, *13*(3), 418. https://doi.org/10.3390/RS13030418

Swales, D. J., Pincus, R., & Bodas-Salcedo, A. (2018). The cloud feedback model intercomparison project observational simulator package: Version 2. *Geoscientific Model Development*, *11*(1), 77–81. https://doi.org/10.5194/GMD-11-77-2018

Team, N. C. (2023). *Ceres energy balanced and filled (EBAF) Toa and surface monthly means data in NETCDF edition 4.2*. NASA Atmospheric Science Data Center. https://doi.org/10.5067/TERRA-AQUA-NOAA20/CERES/EBAF_L3B004.2

Teixeira, J., Wilson, R. C., & Thrastarson, H. T. (2024). Direct observational evidence from space of the effect of CO_2 increase on longwave spectral radiances: The unique role of high-spectral-resolution measurements. *Atmospheric Chemistry and Physics*, *24*(10), 6375–6383. https://doi.org/10.5194/ACP-24-6375-2024

Virtanen, P., Gommers, R., Oliphant, T. E., Haberland, M., Reddy, T., Cournapeau, D., et al. (2020). Scipy 1.0: Fundamental algorithms for scientific computing in python. *Nature Methods*, *17*(3), 261–272. https://doi.org/10.1038/s41592-019-0686-2

Weatherhead, E. C., Reinsel, G. C., Tiao, G. C., Meng, X. L., Choi, D., Cheang, W. K., et al. (1998). Factors affecting the detection of trends: Statistical considerations and applications to environmental data. *Journal of Geophysical Research*, *103*(D14), 17149–17161. https://doi.org/10.1029/98JD00995

Wielicki, B. A., Young, D. F., Mlynczak, M. G., Thome, K. J., Leroy, S., Corliss, J., et al. (2013). Achieving climate change absolute accuracy in orbit. *Bulletin of the American Meteorological Society*, *94*(10), 1519–1539. https://doi.org/10.1175/BAMS-D-12-00149.1